International Journal of Heat and Mass Transfer 176 (2021) 121418

Contents lists available at ScienceDirect

International Journal of Heat and Mass Transfer

journal homepage: www.elsevier.com/locate/hmt

Interaction between flow structure and chemical reaction around the perforated gap of stainless steel–platinum catalytic partition reactor

Yueh-Heng Li*, Kuan-Hsun Peng, Hsiao-Hsuan Kao

Department of Aeronautics and Astronautics, National Cheng Kung University, Tainan 701, Taiwan, R.O.C.

ARTICLE INFO

Article history:
Received 23 November 2020
Revised 1 April 2021
Accepted 25 April 2021
Available online 25 May 2021

Keywords:
Catalytic combustor
Catalytically-stabilized premixed flame
Flame stabilization mechanism
Combined stainless steel–platinum catalytic partition reactor
Combustion efficiency

ABSTRACT

This study investigates the flow structure and chemical reaction around a perforation of a stainless steel–platinum catalytic partition reactor. The small-scale catalytic combustor was partitioned by the combined stainless steel–platinum plate into two channels. Hydrogen/air and methane/air mixtures were individually injected into each channel. The gap provided not only a low-velocity region to stabilize the catalytically-stabilized premixed flame but also a space to exchange the species and radicals diffusing or flowing from both channels, and this led to the inception of gas reaction. The simulation results of the flat catalyst combustor (FCC) and the flat catalytic combustor with a percolated gap (FCG) were compared; the methane/air combustion efficiency of the FCG was found to be much higher than that of the FCC. The reaction around the perforation provided thermal energy and sufficient oxidation radicals to sustain the methane/air flame in the upper channel and further influenced the combustion efficiency and combustion stabilization mechanism. The results indicated that the flame features of the hydrogen/air mixture in the lower channel would affect the flame stabilization mechanism and combustion efficiency of the methane/air mixture in the upper channel. This is due to the imbalance of the temperature and velocity gradients around the perforation.

1. Introduction

The development of microelectromechanical systems (MEMSs) has rapidly progressed in recent years due to the culmination of high-precision fabrication techniques [1]. Microelectromechanical systems enable the miniaturization of mechanical structures and assembly and reduce the overall mass and volume. Generally, MEMSs incorporate microelectronics and micromechanics. They have been intensively applied in portable commodities and electronic gadgets. Nevertheless, the conventional electrochemical batteries, including zinc–air batteries, lithium batteries, and alkaline batteries, feature burdensome weight, low operational life, and high unit cost, leading to the development of high-power-density, hydrocarbon-fueled power sources. Conventional hydrocarbon fuel, with specific energies exceeding 45 MJ/kg, is easily transported, highly safe to use, and relatively cheap. The commercially available lithium/thionyl chloride primary batteries have been reported to have the highest energy density, ~2.6 MJ/kg [2].

The high energy density of hydrocarbon fuels, limited recharging cycles, and long life spans have made microcombustion-based systems more attractive; examples of such systems include microthrusters [3,4], microengines [5], and microreactors [6,7]. Attaining a prolonged flame stabilization in microscale combustors is challenging because of the high surface-area-to-volume ratio. Owing to the smaller size of the combustor, issues regarding the thermal quenching and radical quenching of the flame in a small channel emerge, resulting in increased heat loss and reduced residence time of reactants. However, low combustion efficiency and combustion instability are still two significant challenges in the design of microscale combustors.

These quenching issues are associated with the reduced combustor size. When the heat loss on the wall is greater than the heat generated by flames, the temperature of the reaction zone is reduced, which eventually leads to the retardation or even termination of the overall reaction; this phenomenon is called “thermal quenching” [8]. When some of the highly active molecules or atoms from combustion products collide with the wall, the reaction might be terminated; this phenomenon is called “radical quenching” [9]. The residence time of the reactants must be higher than the time required for the chemical reaction to occur. The residence time of the reactant is proportional to the square of the combustor length. Moreover, the reduced wall temperature, driven by increased heat loss in the microscale combustors, increases the time required for the chemical reactions to complete.

* Corresponding author.
E-mail address: yueheng@mail.ncku.edu.tw (Y.-H. Li).

https://doi.org/10.1016/j.ijheatmasstransfer.2021.121418
0017-9310/

Nomenclature

CFD	Computational Fluid Dynamics
ER	Equivalence ratio, dimensionless
FCC	Flat catalyst combustor
FCG	Flat catalyst combustor with a percolated gap
h	Natural convection heat transfer coefficient, $W/(m^2K)$
MEMs	Microelectromechanical system
q_∞	Heat flux loss to the environment, W
Re	Reynolds number, dimensionless
TPV	Thermophotovoltaic
T_w	The surface temperature of the outer wall, K
T_∞	The temperature of the surrounding, K
$\vec{u}$	Perpendicular velocity component, m/s
$\vec{v}$	Axial velocity, m/s
V	Inlet velocity of fuel and air mixture, m/s
$\dot{v}$	Volume flow rate, m^3/s
Y_{outlet,CO_2}	CO_2 mole concentration at the outlet, dimensionless
Y_{inlet,CH_4}	CH_4 mole concentration at the inlet, dimensionless
Greek	
ε	Emissivity, dimensionless
σ	Stefan-Boltzmann constant 5.67×10^{-8}, $W/(m^2\ K^4)$
η	Combustion efficiency, dimensionless
Subscript	
w	Outer wall
∞	Environment

Numerous popular and competent combustors have been proposed to extend the flame stability limits based on the implementation of flow and heat recirculation techniques; such combustors include the Swiss-roll combustor [10,11], bluff-body combustor [12–16], porous medium combustor [17–19], swirl combustor [20,21], and heat recirculation combustor [15,16,22]. The aforementioned fashions can prolong residence time and preheat the inlet gas, enhancing combustion efficiency [23]. Catalytic combustion is another possible method to sustain flames in small combustion channels by diminishing the chemical reaction time [24–26]. Such combustion can be realized by coating the inner wall of the combustion channel with a thin platinum film [27] or utilizing a platinum-made combustion channel [28]. Kim *et al.* [29] adopted various configurations of the Swiss-roll combustor and assessed the influence of different design parameters on the improvement of flame stabilization, such as the combustor diameter, top plate thickness, channel size, and combustor material. They found that four kinds of coin-sized combustors could successfully sustain a stable flame; moreover, their study demonstrated the feasibility of heat regeneration using a smaller Swiss-roll combustor. Wang *et al.* [30] designed a novel miniature Swiss-roll combustor for non-premixed combustion. The flame could remain stable within a larger range of the equivalence ratio compared with the case of the conventional Swiss-roll combustors, which were prone to flashback at a large equivalence ratio. Wang *et al.* [31] filled a micro-planar combustor with a porous medium to improve thermal performance, which resulted in a higher flame temperature and lower heat loss on the outer wall. The heat loss power was 10.6 W less than that of the free flame combustor at an inlet velocity of 0.6 m/s. Aiming to provide a high and uniform temperature distribution along the combustor walls, Yang *et al.* [32] inserted SiC porous medium foam into a micro-combustor to augment combustion. The wall temperature could increase by at least 90K. The increase in the wall temperature significantly enhanced the radiation energy emitted from the combustor, which is beneficial for electricity generation. He *et al.* [33] proposed a micro-combustor containing a separating cylinder and compared it with the conventional micro-combustor. They found that the existence of the cylinder holder could significantly enhance combustion efficiency. The holder inside the combustor could provide a relatively-low-velocity zone and thus prolong the fuel residence time to improve the combustion efficiency. Through a numerical investigation, Wan *et al.* [34] found that the design of cavities can provide a flow recirculation zone, as well as stabilize the flame and prolong the residence time of the fuel/air mixture.

Applying coating catalysts in the micro-combustion system is a promising method for reducing the thermal and radical quenching and enhancing the reaction to mitigate the radical depletion on the wall [35,36]. Li *et al.* [27,37] proposed a design concept of catalyst segmentation and cavities; here, a low-velocity region is formed, which extends the fuel residence time. Chen *et al.* [38] applied two parallel plates coated with platinum catalysts. The numerical results demonstrated that the hydrogen addition could cause catalytic self-ignition in the micro-channels without startup devices. Wu and Li [37] proposed a conceptual design for the combustion chamber to mitigate critical heat loss and flame instability in a micro-thermophotovoltaic power system [39]. In this design, a platinum tube was employed as a catalyst reactor, and the ring of the percolated hole array on the tube functioned as a fluid-exchange region, providing a channel for fluid exchange between the inner and outer streams. The percolated holes also provided a low-velocity region to increase the fluid residence time. Li and Hong [40] experimentally and numerically examined the flame stabilization mechanism of a platinum reactor with a ring of percolated hole array. The results showed that a hydrogen/air mixture was released in the inner chamber of the platinum reactor; the mixture sustained catalytic combustion inside the chamber and induced the reaction of methane/air mixture in the outer chamber. The numerical results proved that the percolated holes in the combustor could be applied to improve the flammability extension and flame stabilization. Furthermore, hydrogen branched-chain reactions produced enormous amounts of O, H, and OH radicals. These radicals promoted the progressive dehydrogenation of CH_4 to CH_3 and CH_3O, then CH_2O and HCO, and finally, the oxidation of CO to CO_2. The mixture exchange mechanism is that thermal expansion from the surface reaction in the outer chamber propels the mixture toward the inner chamber owing to the nonequilibrium cross-sections of the inner and outer chambers.

Based on a previous study [40], a microreactor was made by only platinum, and the platinum-made microreactor doubled as the emitter for the micro-thermophotovoltaic (μ-TPV) power system [41–44]. The results indicated that the majority of the platinum surface was used for emitting radiation instead of sustaining flames in a microtube. However, platinum is regarded as one of precious metals, and the price of the platinum is too expensive to only use for the emitter of μ-TPV systems. Thus, in the current study, a combined stainless steel–platinum catalytic reactor is proposed to stabilize a micro-flame in a confined space. Here, stainless steel is used to partially replace platinum to reduce material cost without sacrificing combustion efficiency. In addition, employing a catalyst with a perforated gap in the micro-combustor could improve fuel adaptability and operation maneuverability. Understanding the flame stabilization mechanism of the proposed system and optimizing the operational and design parameters are essential.

2. Numerical simulation

Owing to the difficulty of measuring the combustion of the micro-combustor, CFD STARCCM+ software was employed to assess and elucidate the combustion characteristics and flame sta-

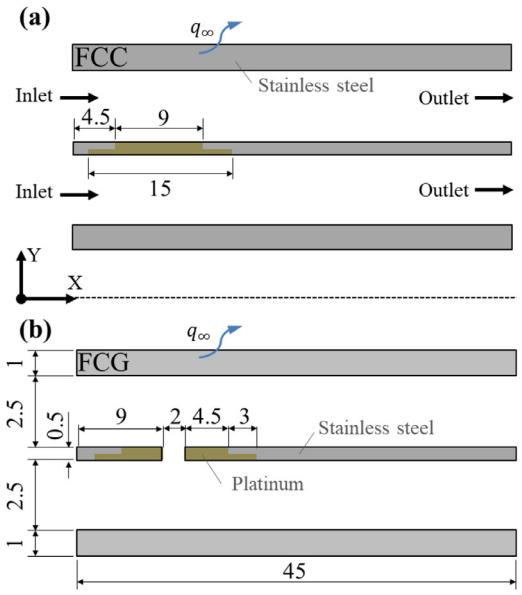

Fig. 1. Dimension of the segmented stainless steel–platinum reactor: (a) without perforated gap; (b) with a perforated gap (unit: mm).

bilization mechanism in the proposed micro-combustion system. The mass, energy, and momentum equations were applied to develop a two-dimensional (2D) and steady-state simulation model. The continuous model and no-slip conditions were acceptable because the Knudsen number was less than 10^{-5} [45]. Moreover, due to the low Reynolds number (Re < 500), the system was regarded as a laminar model. The mixture density was determined by using ideal gas law. Velocity-inlet and pressure-outlet were selected for the boundary condition. The simulation was considered as convergence when the residuals were smaller than 10^{-5}.

To discuss whether the existence of the perforated gap would affect the simulation result, two different segmented stainless steel–platinum combustion systems were employed in this study. One was a combustion chamber partitioned by a catalytic plate without a perforated gap, which was named flat catalytic combustor (FCC). The other was a combustion chamber partitioned by a catalytic plate with a perforated gap, which was named FCC with a percolated gap (FCG). The design of a step-like structure between the stainless steel (AISI 316) and platinum was to make the structure firm. The total length of the combustor was 45 mm, and the wall thickness was 1 mm. The dimension of the perforated gap was 2 mm, and the gap center was 10 mm from the combustor basement. The schematic of the combined stainless steel–platinum catalytic partition reactor, comprising three transversally infinite parallel slabs placed with equidistance of 2.5 mm, is shown in Fig. 1. The heat transfer condition over the combustion wall was concerned with thermal convection and radiation. The methane/air and the hydrogen/air mixtures are injected into the upper and lower channels, respectively. The boundaries of the inlets and outlets are set to the pressure outlet, and the pressure was fixed at 101,325 Pa. The gray blocks indicate the stainless-steel-made combustion wall and the stainless steel portion of the partitioning plate, and the beige blocks present the platinum portion of the partitioning plate in Fig. 1. The heat flux loss (q_∞) to the environment on the combustion wall can be calculated through Eq. (1):

$$q_\infty = h(T_w - T_\infty) + \varepsilon\sigma(T_w^4 - T_\infty^4) \quad (1)$$

where h is the natural convection heat transfer coefficient, 20 W/(m^2 K) [46]; T_w is the surface temperature of the outer wall; T_∞ is the temperature of the surroundings, 300 K; ε is the surface emissivity (stainless-steel: 0.75 [47] and platinum: 0.05 [48]); and σ is the Stefan–Boltzmann constant, 5.67×10^{-8} W/(m^2 K^4). In addition, the thermal conductivities for stainless steel and platinum are 16 and 69.1 W/(m K), respectively; the heat capacities for stainless steel and platinum are 502 and 134 J/(kg K), respectively, and the density for stainless steel and platinum are 8,000 kg/m^3 and 21,450 kg/m^3, respectively.

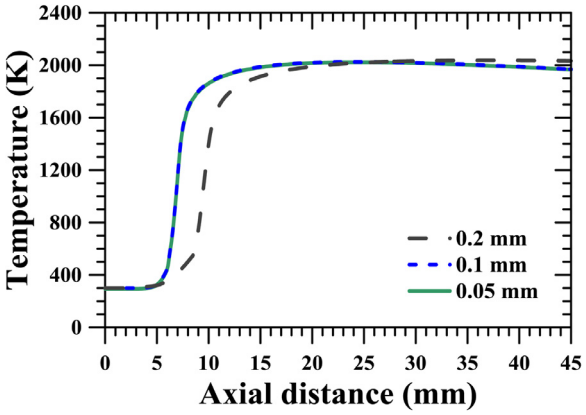

Fig. 2. Mesh independence result.

To describe a detailed homogeneous reaction for the hydrogen/methane/air combustion, the Warnatz gas-phase mechanism [49] was adopted, which consists of 25 species and 108 reaction steps, and the mechanism has been validated in the literature [50,51]. The surface chemistry mechanism over platinum is used by Deutschmann [52]. The simulation includes 11 surface species [H(s), O(s), OH(s), H_2O(s), C(s), CO(s), CO_2(s), CH_3(s), CH_2(s), CH(s), Pt(s)] and 7 gaseous species [CH_4, O_2, H_2, H_2O, CO, CO_2, N_2] as well as 3 radicals [O, OH, H], where nitrogen is a chemically inert species, and 24 reaction steps. Reinke *et al.* [51] used the above mechanism to evaluate the homogeneous ignition point and compared the experimental and numerical results. It appears that the numerical results were consistent with the experimental results. In addition, the selected gas and surface mechanisms have been intensively employed in the study of the combustion behavior of microreactors [35,37,53–55]. In the current study, the chemical mechanism was employed to simulate the hydrogen/methane premixed flame in the catalytic combustion system.

For the simulation accuracy, a grid-independent test was performed before the analysis. Three meshes of different sizes were tested: 0.05 mm, 0.1 mm, and 0.2 mm. Fig. 2 shows the mesh independence result. According to the temperature distribution at the centerline of the lower channel, the rougher the grid size, the larger the deviation. However, the temperature distributions of the grid size 0.05 mm and 0.1 mm followed a similar trend. When the base size of the mesh was reduced to 0.05 mm, more computational time was required, and the result was hard to converge. Therefore, a 0.1 mm grid was adopted in this study.

3. Studying system operating parameters of the catalytic partition reactor

3.1. Effect of the perforation presence

The perforation in the catalyst is intended to provide a relatively low location to anchor flames by trading off thermal energy and radicals between two channels. To scrutinize the effect of the perforation presence on flame stabilization and combustion efficiency, FCC and FCG conducted the simulation with identical flow conditions, which are 5 m/s of the methane/air mixture in the upper channel and 10 m/s of the hydrogen/air mixture in

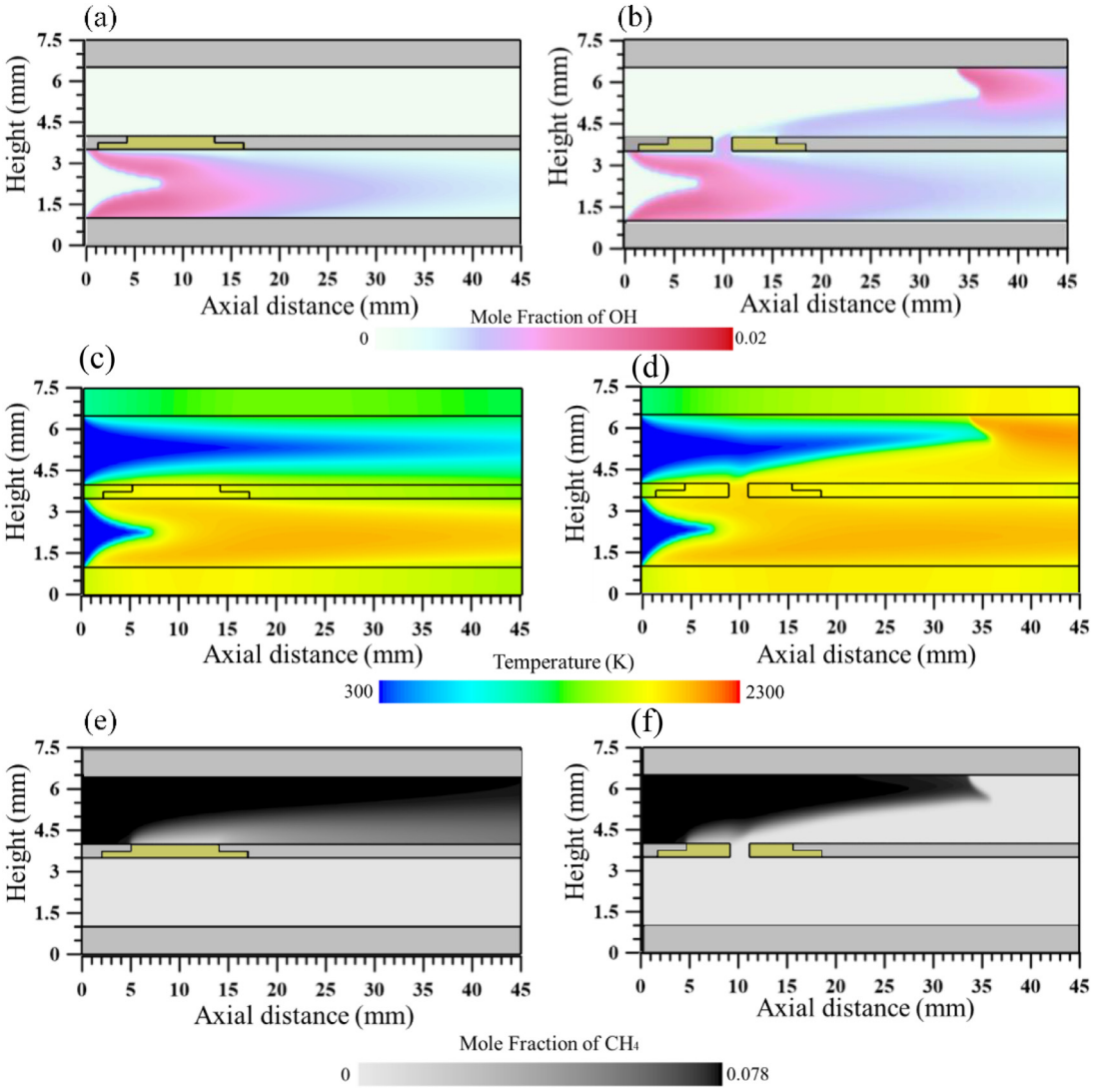

Fig. 3. Mole fraction of (a, b) OH mole fraction, (c, d) temperature distribution, (e, f) CH_4 mole fraction distribution in the FCC and FCG cases.

the lower channel, respectively. The overall equivalence ratios in two channels were set to 0.8. The material of the combustor wall was stainless steel, and the heat transfer coefficient was 20 W/(m^2 K). Fig. 3(a, b) displays the OH mole fraction, (c, d) displays the temperature distribution, and (e, f) displays the CH_4 mole fraction distribution along the combustor for FCC and FCG. In Fig. 3(a, b), this proves that the hydrogen/air mixture is prone to ignition in the lower channel, and the hydrogen/air premixed jet flame is anchored in the upstream region in both FCC and FCG cases. In the upper channel, no OH mole fraction is distributed in the FCC case. Arguably, no gas reaction occurred in the upper channel in the FCC case. Nonetheless, in the FCG case, OH mole fraction anchoring can be observed in the perforation and trailing towards the downstream region. Evidence suggests that the gas reaction of the methane/air mixture was sustained in the upper channel in Fig. 3(b). Comparing the temperature distribution on combined stainless steel–platinum partitioning plate in Fig. 3(c, d), the result signifies that the platinum plate inherited the thermal energy from the exothermicity of both hydrogen/air homogeneous and heterogeneous reactions. However, the heated platinum plate could not induce the gas reaction of the methane/air mixture in the counterpart channel in the FCC case. One can infer from the methane mole fraction in Fig. 3(e) that methane was slightly consumed at the platinum section, and this methane consumption can be attributed to the surface reaction of methane. For the FCG case, methane was not only consumed at platinum surfaces but also enormously depleted in the vicinity of the perforation and the downstream stainless-steel section, as illustrated in Fig. 3(f). The numerical results illustrate that the perforation helps to induce catalytically stabilized combustion in the methane/air channel, which elevates the combustion efficiency of the methane/air mixture.

Fig. 4 illustrates the velocity distribution along the upper and lower surfaces of the catalytic partitioning plate. The positive velocity magnitude denotes that the velocity flows in the y^+ direction, and the negative value denotes the velocity flowing in the y^- direction. The gray areas denote the locations of catalytic surface segmentation. Fig. 4(a) illustrates a negative velocity $\vec{v}$ in the FCG case, indicating the penetration of gas mixture from the upper channel to the lower channel through the perforation. The velocity $\vec{v}$ distribution in the FCC case near the upper surface of the catalytic partitioning plate is zero because the system has no gap on the partitioning plate and no intervening inflow stream from the counterpart channel. In addition, a small peak located at the front edge of the second platinum plate could be caused by the recirculating flow of the outbound methane/air mixture or the combustion product of the lower channel penetrating the upper channel.

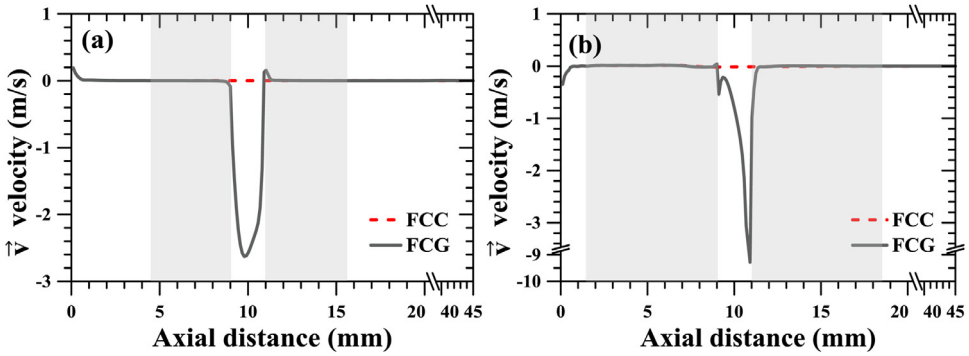

Fig. 4. Distribution of the velocity $\vec{v}$ with (a) upper and (b) lower surfaces of the partitioning plate.

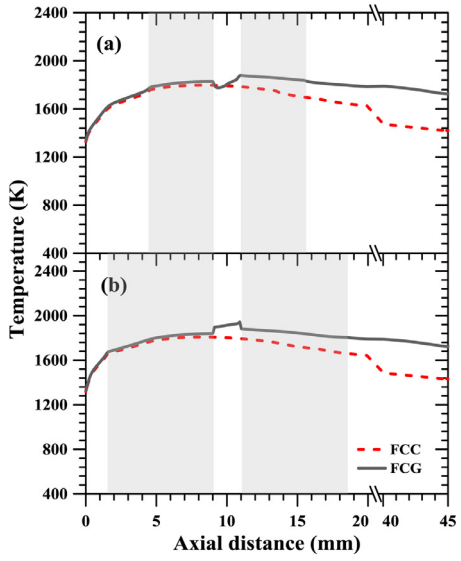

Fig. 5. Temperature distribution along with (a) upper and (b) lower surfaces of the catalytic partitioning plate.

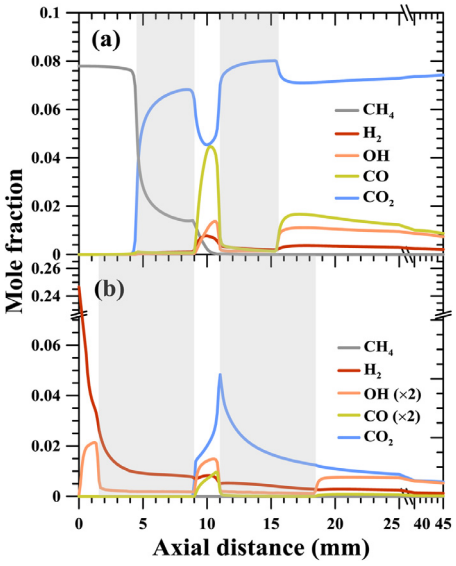

Fig. 6. Fuel and radical mole fractions with (a) upper and (b) lower surfaces of the partitioning plate for $V_{CH4/air}$ = 5 m/s and $V_{H2/air}$ = 10 m/s.

Fig. 4(b) illustrates the two significant negative peaks of the velocity $\vec{v}$ distribution in the FCG case. Evidence indicates that the gas mixture in the perforation flows into the lower channel. Compared with the results of the FCC case, the FCG case has a high interaction between the two partition channels and the perforation. The flow interdependency between the two partitioning channels is essential to maintain the flame stabilization in the confined space.

Fig. 5 illustrates the temperature distribution along the upper and lower surfaces of the catalytic partitioning plate. The results prove similar temperature distributions in the first stainless steel-platinum sections (anterior to the perforation) of the FCC and FCG cases, but not in the second stainless steel-platinum section (posterior to the perforation). It appears that the heterogeneous reaction over the platinum in both FCC and FCG cases commences. However, the ensuing homogeneous reaction only sustains itself in the FCG case, but not in the FCC case. The gradual increase of the temperature in the FCG case explains the presence of an induced homogeneous reaction of the methane/air mixture sustained near the partitioning plate.

Fig. 6 illustrates the species and radical mole fractions along the axial direction close to the upper and lower surfaces of the reactor for $V_{CH4/air}$ = 5 m/s and $V_{H2/air}$ = 10 m/s. For the upstream region of the lower channel, Fig. 6(b) illustrates the onset of hydrogen consumption and radical hydroxyl production on the surface of the first stainless-steel section. This implies that the gas reaction is induced and anchored on the first stainless-steel surface of the lower channel. This is because the surface reaction on the following platinum provides thermal energy to the upstream stainless-steel section and sustains the gas reaction. In the perforation, hydrogen is completely consumed. The produced carbon monoxide and carbon dioxide are present in the perforation. The methane or hydrocarbon species in the upper channel penetrates to the lower channel and induces the gas reaction, leading to the production of CO and CO_2. In Fig. 6(a), the heterogeneous reaction of methane commences on the first platinum surface and fully consumes itself in the vicinity of the perforation. Furthermore, the hydroxyl mole fraction is obvious in the perforation of the upper channel, as illustrated in Fig. 6(a). This implies the existence of gas reaction of the methane/air mixture, tailing towards the downstream region of the upper channel. Behind the second platinum section, the system has OH, H_2, CO, and CO_2 mole fraction distributions. The resulting H_2 is the intermediate species of the methane/air gas reaction and is not diffused from the lower channel. It is because that an oxidation radial (O, H, OH) pool was sustained in the perforation. These radicals facilitate the progressive dehydrogenation of CH_4 to CH_3 and CH_3O, then to CH_2O, HCO, and finally oxidation of CO to CO_2 in the upper channel.

3.2. The effect of the catalyst layout and fuel/air deployment

The result above showed that the perforation in the catalyst provides a relatively low location to anchor flames by trading off

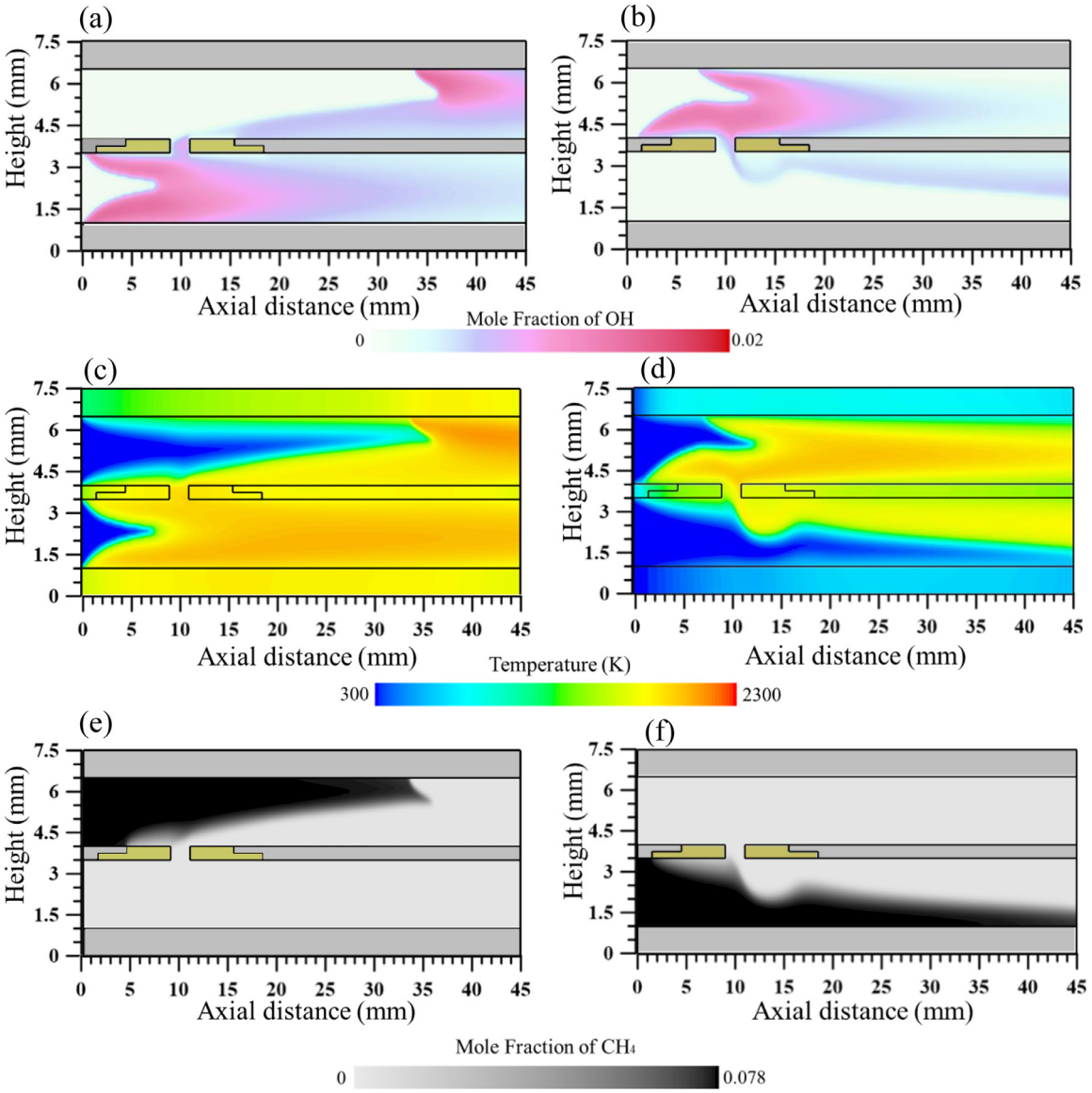

Fig. 7. Mole fraction of (a, b) OH mole fraction, (c, d) temperature distribution, (e, f) CH_4 mole fraction distribution in the two different fuel/air mixture deployments.

thermal energy and radicals between two channels. The hydrogen/air flame anchored on the first stainless steel section of the partitioning plate due to the onset of catalytic combustion over the ensuing platinum section of the partitioning plate. Presumably, the platinum length plays an important role in a flame anchoring position. In order to examine the effect of catalyst length on the flame anchoring position of the hydrogen/air and methane/air mixture, the fuel/air deployment was rearranged accordingly. That is to say, the hydrogen/air mixture was injected into the upper section, whereas the methane/–air mixture was injected into the lower section.

Fig. 7 illustrates OH mole fraction, temperature distribution, and methane mole fraction distribution in two different fuel/air deployments. The flow velocity conditions were 5 m/s for the methane/air mixture and 10 m/s for the hydrogen/air mixture. The overall equivalence ratios in two channels were set to 0.8. Fig. 7(a, c, e) represents the condition of the hydrogen/air mixture injected into the lower section and the methane/air mixture injected into the upper section. On the contrary, the hydrogen/air mixture was injected into the upper section, and the methane/air mixture injected into the lower section for Fig. 7(b, d, f). The effective platinum length facing toward the mainstream in the upper channel is 9 mm, and the effective platinum length in the lower section is 15 mm. Fig. 7(a, b) demonstrates the significant difference of OH mole fraction distribution for the hydrogen/air mixture and the methane/air mixture. In Fig. 7(b), the flame potential cone of the hydrogen/air mixture is asymmetrical, and the flame anchoring position on the combustion chamber would recede toward the downstream due to the thermal quenching and heat loss on the wall. However, the flame potential cone of the hydrogen/air mixture in Fig. 7(a) is more symmetrical. For the methane/air mixture, the flame anchoring position anchors on the perforation in two cases. In Fig. 7(b), the asymmetrical flame cone promotes the penetration of gas mixture from the upper section into the lower section, leading to a recirculation zone adhered to the platinum section of the second partitioning plate (hereafter referred to as the second platinum plate). It is like a boundary layer premixed flame stabilized over a surface in the lower section of Fig. 7(b). In addition, regarding temperature distribution, it is obvious to discover that the high-temperature zone in the upper channel of the hydrogen/air mixture in Fig. 7(d) shrinks compared to the lower channel of the hydrogen/air mixture in Fig. 7(c). Basically, the quantity of

Table 1
The combustion efficiency values of the methane/air mixture with respect to various inlet ratios in FCC and FCG conditions.

	FCC	FCG	FCC	FCG	FCC	FCG
$V_{CH4/air}$ (m/s) / $V_{H2/air}$ (m/s)	5/10		6/12		7/14	
$\eta_{CH_4/air}$ (%)	7.5	91.6	6.58	81.3	5.68	62.3

hydrogen/air injection is identical in two cases, and all hydrogen is entirely consumed. Consequently, the temperature distribution of the hydrogen/air mixture is supposed to be similar in Fig. 7(c, d). However, the fact of the distinct temperature distribution in the combustion channel of the hydrogen/air mixture in these two cases implies the flow interaction of the fuel/air mixture through the perforation. The change of flame anchoring mode deteriorates the methane conversion in the counterpart channel in Fig. 7(f). Apparently, there is a certain unburnt methane mixture remaining in the lower section. It is anticipated that the flame anchoring mechanism is associated with the flame behavior patterns of the fuel/air mixture presented in two channels.

The numerical results reveal that the hydrogen/air mixture is prone to undergo complete combustion in the combustion channel, unlike the methane/air mixture. Therefore, to examine the combustion efficiency of the methane/air mixture is an iconic indicator to assess the overall combustion efficiency with regard to various operational conditions. The combustion efficiency (η) of the methane/air mixture can be determined by using Eq. (2), which is the ratio of the volumetric flow rate of produced carbon dioxide at the outlet to the volumetric flow rate of injected methane at the inlet.

$$\eta_{CH_4/air} = \frac{\dot{\mathcal{V}}_{outlet} \times Y_{outlet,CO_2}}{\dot{\mathcal{V}}_{inlet} \times Y_{inlet,CH_4}}, \quad (2)$$

where $\eta_{CH_4/air}$ is the combustion efficiency of the methane/air mixture, Y_{outlet,CO_2} is the produced CO_2 mole concentration at the outlet, Y_{inlet,CH_4} is the CH_4 mole concentration at the inlet, and $\dot{\mathcal{V}}$ is the volumetric flow rate of the inlet and outlet. Therefore, the $\eta_{CH_4/air}$ for the hydrogen/air mixture in the lower section and the methane/air mixture in the upper channel is 91.6%. On the contrary, the $\eta_{CH_4/air}$ for the hydrogen/air mixture in the upper channel, and the methane/air mixture in the lower channel is 58.8%.

3.3. The inlet velocity effect of the methane/air and hydrogen/air mixture

A hydrocarbon–air mixture is difficult to sustain in the micro-combustor due to the low residence time and high heat loss on the wall. Increasing the inlet velocity of the fuel tends likewise to increase the overall quantity of fuel injection. The inlet velocity of the fuel/air mixture affects the residence time, and the resulting fuel concentration influences the chemical reaction time in the micro-combustor. Furthermore, the velocity gradient in the vicinity of the perforation would affect the fluid dynamic interdependency of the flow streams in the two parallel channels. To examine the underlying issue, such as the correlation between the flame stabilizing position and the flow velocity in the two channels, three flow velocity sets of the methane/air mixture and hydrogen/air mixture were designed, namely 5 m/s and 10 m/s, 6 m/s and 12 m/s, as well as 7 m/s and 14 m/s. The velocity ratio of the methane/air mixture to the hydrogen/air mixture was fixed. Table 1 presents the combustion efficiency of the methane/air mixture with respect to various ratios in the FCC and FCG cases. The combustion efficiencies of the methane/air mixture for all FCC cases are certainly low, and the resulting values are less than 10%. This implies no commencement of the methane/air gas reaction in the upper channel. However, the combustion efficiencies

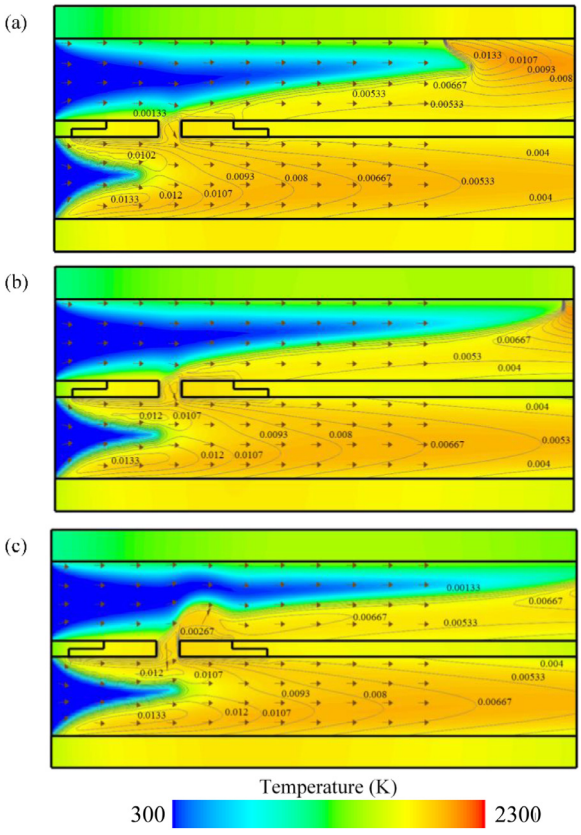

Fig. 8. Temperature distribution overlaid with OH mole fraction and velocity vector for (a) $V_{CH4/air}$ = 5 m/s and $V_{H2/air}$ = 10 m/s, (b) $V_{CH4/air}$ = 6 m/s and $V_{H2/air}$ = 12 m/s, (c) $V_{CH4/air}$ = 7 m/s and $V_{H2/air}$ = 14 m/s.

of the methane/air mixture in all FCG cases gradually decreased from 91.6% for $V_{CH4/air}$ = 5 m/s and $V_{H2/air}$ = 10 m/s to 62.3% for $V_{CH4/air}$ = 7 m/s and $V_{H2/air}$ = 14 m/s, as listed in Table 1.

In general, the combustion efficiency of the methane/air mixture decreases with the increase of the fuel/air flow velocity. Fig. 8 illustrates the temperature distribution overlaid with the OH mole fraction and velocity vector under different inlet velocity conditions when the equivalence ratio for the methane/air and hydrogen/air mixtures is 0.8. The results indicated that the flame cone of the hydrogen/air mixture does not significantly change in three flow velocities of the fuel/air mixture. On the contrary, the flame basement of the methane/air mixture anchors on the upper wall and in the perforation in the case of $V_{CH4/air}$ = 5 m/s and $V_{H2/air}$ = 10 m/s. Depending upon the increasing flow velocity of the fuel/air mixture, the flame anchoring position of the methane/air mixture appears to stand still in the perforation, but the flame anchoring position on the upper wall tends to recede to the channel exit when the flow velocity reaches $V_{CH4/air}$ = 7 m/s and $V_{H2/air}$ = 14 m/s.

Fig. 9 presents an enlarged image to illustrate the flow direction in the area of the perforation. Owing to the high velocity distributed in the vicinity of the perforation near the lower surface of the partitioning plate, the gas mixture in the upper channel would flow into the lower section. The streamline of the gas mixture in the upper channel clearly trespasses towards the lower section in the case of $V_{CH4/air}$ = 5 m/s and $V_{H2/air}$ = 10 m/s. The flame anchoring position of the methane/air mixture leashes in the perforation. The details of the flame stabilizing mechanism with various inlet velocity conditions are discussed in Section 4. The corresponding value of $\eta_{CH_4/air}$ reached 91.6%, as listed in Table 1.

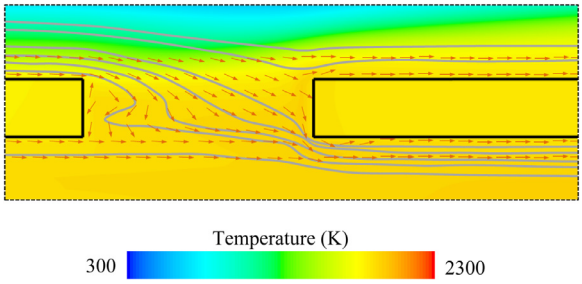

Fig. 9. Temperature distribution overlaid with velocity vector and streamline for $V_{CH4/air}$ = 5 m/s and $V_{H2/air}$ = 10 m/s around the perforation.

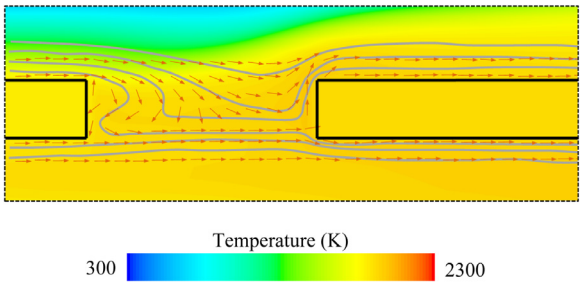

Fig. 10. Temperature distribution overlaid with velocity vector and streamline for $V_{CH4/air}$ = 6 m/s and $V_{H2/air}$ = 12 m/s around the perforation.

When the fuel/air flow velocities reach $V_{CH4/air}$ = 6 m/s and $V_{H2/air}$ = 12 m/s, the methane/air mixture would flow into the perforation but does not penetrate the lower channel. The inflow stream from the upper channel would enter the perforation and sequentially turn back instead, as illustrated in Fig. 10. It seems that the increase of the hydrogen/air inlet velocity increases hydrogen injection quantity in the lower channel. The increasing hydrogen concentration enhances the chemical reaction of hydrogen combustion. The hydrogen/air premixed flame would gradually increase and expand in the vicinity of the perforation in the lower channel. The growth of the hydrogen/air premixed flame would accelerate the flow velocity of the gas mixture and increase the localized pressure nearby the perforation in the lower channel. This would lead to barricading against the penetration of the gas mixture from the upper channel. This phenomenon resembles fluid flowing into a cavity, as illustrated in Fig. 10.

Fig. 11 illustrates fuel and radical mole fractions along with the upper and lower surfaces of the catalytic partitioning plate for $V_{CH4/air}$ = 6 m/s and $V_{H2/air}$ = 12 m/s. Due to the different flow directions, the gas mixture in the perforation returns to the upper channel. The peak value of CO_2 mole fraction in the lower channel is two times smaller than that for $V_{CH4/air}$ = 5 m/s and $V_{H2/air}$ = 10 m/s. The quantities of CO and CO_2 in the lower surface of the catalytic partitioning plate are smaller than those for $V_{CH4/air}$ = 5 m/s and $V_{H2/air}$ = 10 m/s. This happens because the flow velocity in the upper channel increases and the residence time in the perforation reduces, leading to a lower $\eta_{CH_4/air}$. The $\eta_{CH_4/air}$ for the case of 6 m/s $V_{CH4/air}$ and 12 m/s $V_{H2/air}$ drops to 81.3% compared with that for $V_{CH4/air}$ = 5 m/s and $V_{H2/air}$ = 10 m/s.

However, when the fuel/air condition reaches $V_{CH4/air}$ = 7 m/s and $V_{H2/air}$ = 14 m/s, the gas mixture in the lower section flows into the perforation and then penetrates the upper channel, as illustrated in Fig. 12. Owing to the increase of inlet hydrogen injection quantity in the lower section, the hydrogen/air premixed flame expands and forces the gas mixture into the upper channel through the perforation. The interaction between the two gas streams from the upper and lower channels forms a circulation

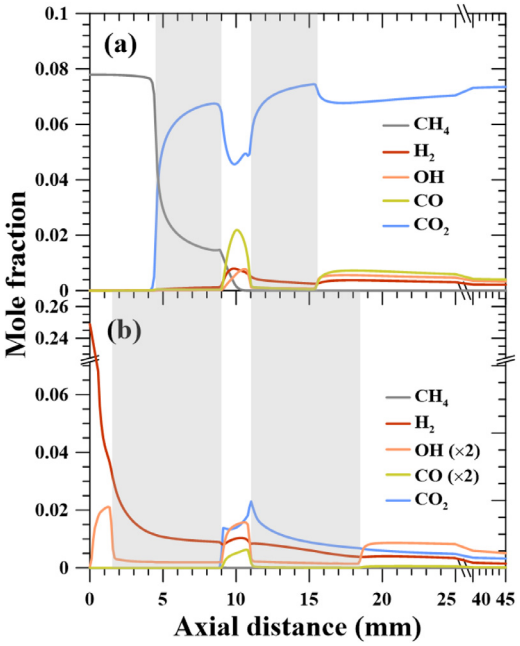

Fig. 11. Fuel and radical mole fractions with (a) upper and (b) lower surfaces of the catalytic partitioning plate for $V_{CH4/air}$ = 6 m/s and $V_{H2/air}$ = 12 m/s.

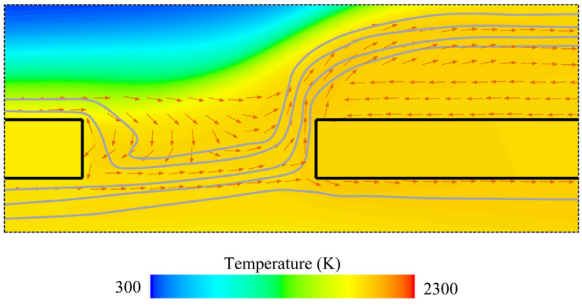

Fig. 12. Temperature distribution overlaid with velocity vector and streamline for $V_{CH4/air}$ = 7 m/s and $V_{H2/air}$ = 14 m/s around the perforation.

zone that is sustained on the second platinum plate. The circulation zone can be observed on the second platinum plate in Fig. 12.

Fig. 13 illustrates the fuel and radical mole fractions with the upper and lower surfaces of the catalytic partitioning plate for $V_{CH4/air}$ = 7 m/s and $V_{H2/air}$ = 14 m/s. The CO and CO_2 mole fractions in the upper surface of the catalytic partitioning plate are low compared with those of Fig. 13(a). The existence of the circulation zone in the second platinum plate defers the homogeneous and heterogeneous reaction of CO. Fig. 14 also illustrates the spatial distribution of CO mole fraction in the vicinity of the perforation. The results indicate the resulting CO detours, which follow the boundary of the recirculating bubble and are homogeneously consumed in the downstream region of the upper channel. Therefore, the product CO_2 mole fraction in the vicinity of the second platinum plate is low.

Fig. 15 illustrates the velocity $\vec{u}$ distribution along with the upper surface of the catalytic partitioning plate. Along with the second platinum section, it appears that the quantity of velocity $\vec{u}$ is negative. The reattachment point can be found at velocity $\vec{u}$ equal to zero, *that is*, located at x = 15 mm. Therefore, the reattachment length, also known as the overall length of the recirculating bubble, is 4 mm, covering the major area of the second platinum plate. The presence of the recirculating bubble anchoring not only obstructs the mixing ability of two streams from the upper and lower chan-

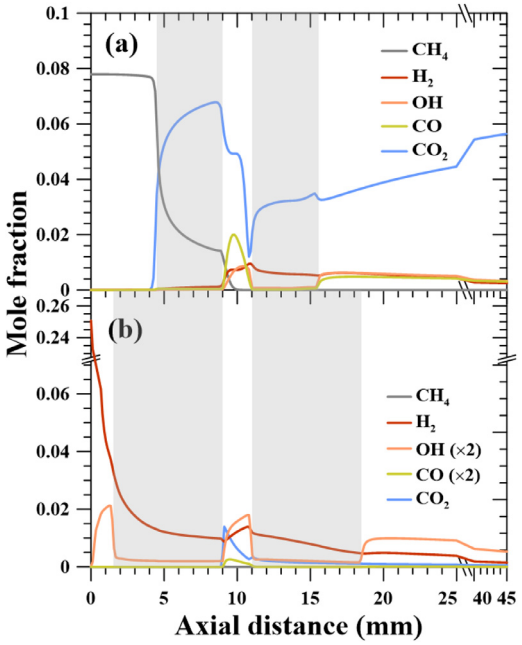

Fig. 13. Fuel and radical mole fractions with (a) upper and (b) lower surfaces of the catalytic partitioning plate for $V_{CH4/air}$ = 7 m/s and $V_{H2/air}$ = 14 m/s.

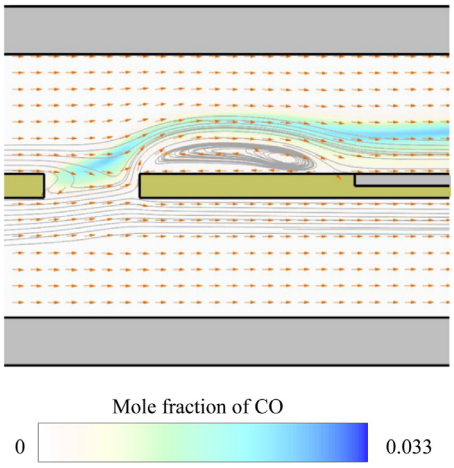

Fig. 14. CO mole fraction overlaid with velocity vector and streamline for $V_{CH4/air}$ = 7 m/s and $V_{H2/air}$ = 14 m/s around the perforation.

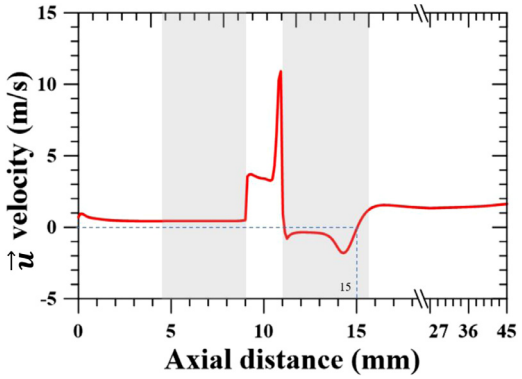

Fig. 15. Distribution of the velocity $\vec{u}$ along with the upper surface of the catalytic partitioning plate.

nels but also diminishes the probability of heterogeneous reaction of derived hydrocarbon species over the second platinum plate. Consequently, the $\eta_{CH_4/air}$ of this case with 7m/s $V_{CH4/air}$ and 14 m/s $V_{H2/air}$ is only 62.3%.

3.4. The equivalence ratio effect of the methane/air and hydrogen/air mixture

Fig. 16 shows the CO mole fraction distribution overlaid with OH mole fraction contours in different equivalence ratios when the inlet velocities of the methane-air mixture in the upper channel and the hydrogen/air mixture in the lower section are 6 and 12 m/s, respectively. It can be seen that, as the equivalent ratio of the hydrogen/air mixture decreases, the flame phenomenon changes significantly, especially the flame anchoring position of the methane-air mixture in the upper channel. For example, the equivalence ratio of the methane-air mixture is fixed 0.8; the gas mixture from the upper section would flow into the perforation and penetrate the lower section as the stoichiometric condition of the hydrogen/air mixture. At present, the $\eta_{CH_4/air}$ of this condition achieves 85.8%. But when the equivalence ratio of the hydrogen/air mixture reduces to 0.6, the gas mixture from the lower section would reversely flow into the perforated gap and penetrate the upper channel. There is an evident recirculation bubble laid on the second platinum plate. The corresponding $\eta_{CH_4/air}$ reduces to 50.9%. Based on the previous speculation, the presence of the recirculation bubble would deteriorate the $\eta_{CH_4/air}$. Especially when $ER_{H2/air}$=0.6, the recirculation bubbles emerge for all $ER_{CH4/air}$.

Fig.17 displays the distribution of the velocity $\vec{u}$ along with the upper surface of the catalytic partitioning plate. It is convenient to determine the reattachment length of three conditions, namely, 15.78 mm for $ER_{CH4/air}$ =1.0, 16.20 mm for $ER_{CH4/air}$ =0.8, 16.65 mm for $ER_{CH4/air}$. The corresponding $\eta_{CH_4/air}$ present 60.8% mm for $ER_{CH4/air}$ =1.0, 50.9% mm for $ER_{CH4/air}$ =0.8, 36.3% mm for $ER_{CH4/air}$ =0.6. It confirms that the larger reattachment length of the recirculation bubble is associated with the lower combustion efficiency of the methane-air mixture.

4. Flame stabilizing mechanism

4.1. The flow penetration of methane/air derived gas mixture

As aforementioned, the variation of inlet velocity and fuel/air equivalence ratio would influence the flow structure inside the percolated gap. However, different flow structures would result in different flame stabilizing positions of the methane/air mixture. In general, two distinct flame stabilization mechanisms operated according to the coupled flow structures between the two streams from the upper and lower channels. Typically, some prerequisites are required to sustain the flame anchoring basement of the fuel/air premixed flame, such as a provision of a regime with a relatively low flow velocity but a high-temperature field, along with the support of a sufficient fuel/air mixture and oxidizing radical species. Accordingly, the first flame stabilization mechanism of the methane/air mixture emerges when the gas mixture penetrates from the upper channel (the channel filled with the methane/air mixture) to the lower channel (the other channel filled with the hydrogen/air mixture). This flame stabilization mechanism features the unburnt hydrocarbon species and the fuel-derived radicals (e.g., CH_3, CH_2, and CH) congregating in the asylum-like perforation to support a catalytically-induced gas reaction with the help of catalyst facilitation and the thermal provision from the nearby oxidation of the hydrogen–air mixture. The first type of flame stabilizing mechanism can be observed when inlet velocity condition of the methane/air mixture is equal to 5 m/s, and that of the hydrogen/air mixture is equal to 10 m/s. The equivalence ratios in two

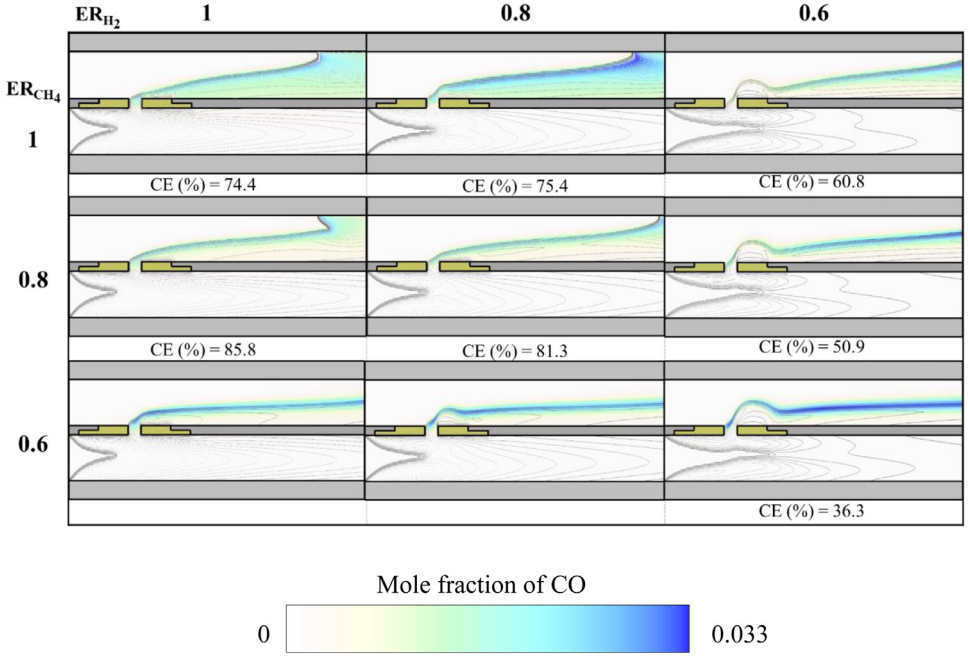

Fig. 16. CO mole fraction distribution overlaid with OH mole fraction for different inlet equivalence ratios.

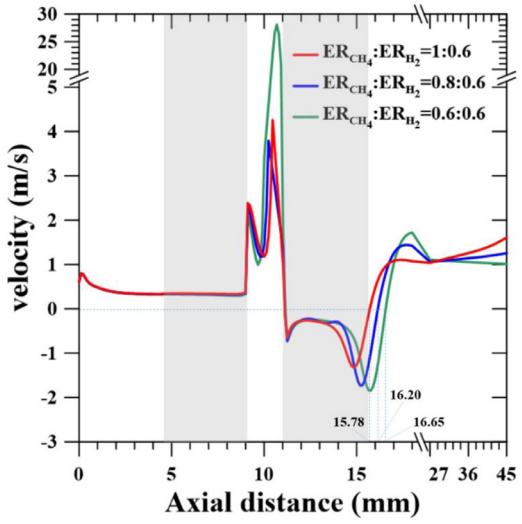

Fig. 17. Distribution of the velocity ū with the upper surface of the catalytic partitioning plate.

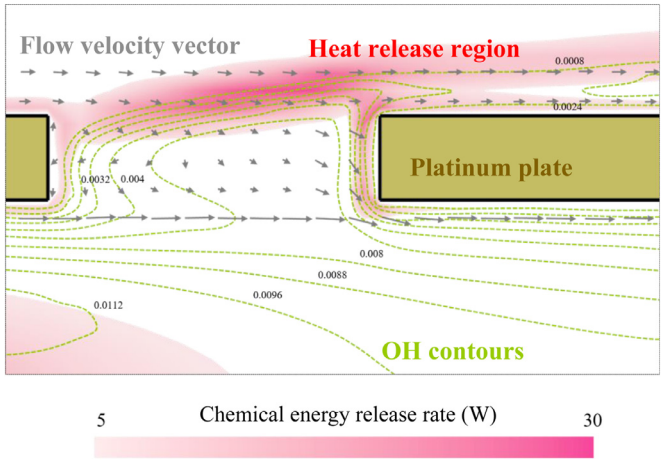

Fig. 18. Heat release overlaid with velocity vectors and OH mole fraction contours around the perforation.

channels are fixed at 0.8, the wall material of the combustor wall is stainless steel, and the heat transfer coefficient is 20 W/(m^{2}K). Fig. 18 illustrates the heat release overlaid with the velocity vector and OH mole fraction in the vicinity of the perforation. The figure shows that a high heat release region, denoted by a white and red binary color legend, was capped on the top surface of the perforation. The velocity vectors imply that the gas mixture in the upper channel flows into the perforation. Moreover, the inflow stream carries unburned hydrocarbon fuels and fuel-derived radicals into the perforation. However, the catalyst wall on the two side walls of the perforation can effectively facilitate the catalytically induced gas reaction. A significant heat release appears close to the catalyst sidewalls of the perforation. The dashed line contours denote OH mole fraction distributions and reveal the location of gas reaction occurrence in the perforation. In addition, most hydroxyls are diffused from the lower channel, which is provided by the gas reaction of the hydrogen–air mixture. Generally, the first platinum plate initiates the degradation of the inflow methane, leading to the yield of fuel-derived species and radicals. Those fuel-derived species and radicals were carried into the perforation and reacted in situ with oxidizing radicals diffused from the lower channel. A portion of inflow fuel-derived species and radicals penetrate into the lower channel and then reacted in the lower channel. Consequently, the flame basement of the methane/air mixture extended to the perforation and the lower channel. This flame stabilization mechanism was undoubtedly stable and accompanied by a high $\eta_{CH_4/air}$ of the methane/air mixture. The heat release region in the upstream zone indicated that the hydrogen/air mixture reacted in the upstream zone.

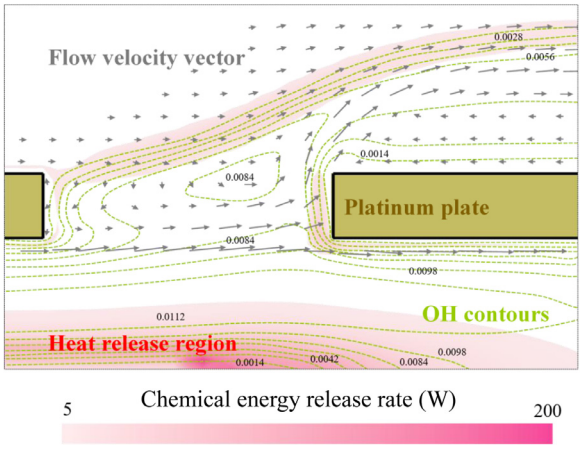

Fig. 19. Heat release overlaid with velocity vector and OH mole fraction around the perforation.

4.2. The flow penetration of hydrogen/air derived gas mixture

The second flame stabilizing mechanism of the methane/air mixture emerges in consequence of the gas mixture penetrating from the lower channel (the channel filled with the hydrogen/air mixture) to the upper channel (the other channel filled with the methane/air mixture). In this flame stabilization mechanism, the flame sheet of the methane/air mixture was elevated due to the inception of the recirculation bubble sustained in the second platinum plate. However, the presence of the recirculation bubble would defer the entrance of unburned hydrocarbon fuel towards the second platinum plate and jeopardize the catalytic reaction in the upper channel. The unburned hydrocarbon species and fuel-derived radicals could not access the second platinum plate and were accelerated by the outer boundary of the recirculation zone. The elevated velocity vectors revealed that the unburned hydrocarbon species and fuel-derived radicals were accelerated, leaving the platinum section. This resulted in flame instability and low combustion efficiency for the methane/air mixture. The second type of flame stabilizing mechanism can be observed with the velocity condition of the methane/air mixture equal to 7 m/s and that of the hydrogen/air mixture equal to 14 m/s. The equivalence ratios in two channels are fixed at 0.8. Fig. 19 illustrates the heat release overlaid with the velocity vector and OH mole fraction around the perforation. Compared with Fig. 18, the main difference is the appearance of a high heat release region in the lower channel. This was because the high hydrogen concentration injected into the lower channel intensified the gas reaction of the hydrogen/air mixture. The flame sheet of the hydrogen/air flame was extended, and it barricaded against the penetration of the gas mixture from the upper channel. Instead, the gas mixture from the lower channel was pushed to enter into the perforation and the upper channel. The interaction between the incoming flow streams from the upper and lower channel formed a recirculation bubble, which was sustained in the second platinum plate. The onset of the recirculation bubble was associated with the flow structure alternation in the perforation.

Fig. 20 illustrates the CO mole fraction overlaid with streamline around the perforation. The presence of the recirculating bubble not only obstructed the mixing ability of two streams from the upper and lower channels but also diminished the probability of a heterogeneous reaction of derived hydrocarbon species over the second platinum plate. Furthermore, the reattachment length of the recirculation bubble was pertinent to the hydrogen inlet concentration and equivalence ratio of the hydrogen/air mixture in the channel.

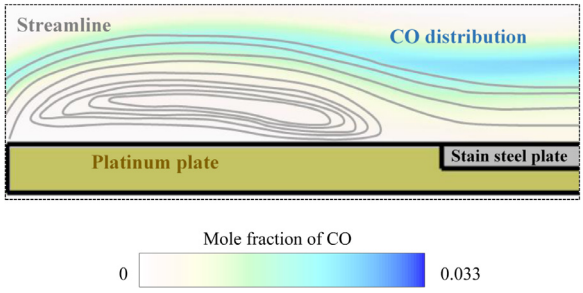

Fig. 20. CO mole fraction overlaid with streamlines around the perforation.

5. Approaches to improve flame stabilization and combustion efficiency

The parameters, such as inlet velocity and equivalence ratio, affected the flame stabilizing mechanism and the overall combustion efficiency. However, the flame stabilizing mechanism is relevant to the flow structure within the perforation. The imbalance of the thermal gradient and velocity gradient on the peripheral side of the perforation causes the alternation of the flame stabilizing mechanism and affects the $\eta_{CH_4/air}$. Therefore, two implementations can curtail the effect of the presence of the perforation on the flow structure and combustion behavior. First, the location of the perforation moves towards the downstream region. The perforation was placed in the upstream region close to the anchoring position of the methane/air mixture. The fluctuations in flow velocity, temperature, and pressure near the perforation would deteriorate and undermine the flame stabilization of the methane/air mixture, leading to a reduction in $\eta_{CH_4/air}$. Consequently, relocating the perforation position in the downstream is a plausible approach to ameliorate the low combustion efficiency. Second, reducing the dimension of the perforated gap could retard the sensitivity of velocity fluctuations to the flame stabilization of the methane/air mixture. To examine these two implementations, the effects of the perforation position and dimension on the combustion behavior of the methane/air mixture were investigated.

Fig. 21 illustrates the temperature distribution overlaid with OH mole fraction and velocity vector in different perforation positions (x = 10, 20, 30 mm) when the inlet velocities of the methane/air mixture and hydrogen/air mixture are 6 and 12 m/s, respectively. The equivalence ratios for all fuel/air mixtures are 0.8, and the heat transfer coefficient is 20 W/(m^2 K). A distinct difference in the combustion phenomenon was observed when the location of the perforation moves to the middle stream or downstream.

When the perforation position is at x = 10 mm, the flame stabilization of the methane/air mixture anchoring is easy to identify in the perforation, as illustrated in Fig. 21(a). The corresponding $\eta_{CH_4/air}$ reached 81.3%, as listed in Temperature distribution overlaid with OH mole fraction and velocity vectors in different perforation positions: (a) 10 mm, (b) 20 mm, (c) 30 mm.. Nonetheless, when the perforation position was moved to the middle stream or downstream sections at x = 20 and 30 mm, respectively, the flame anchoring position of the methane/air mixture stabilized on the first stainless-steel section, as illustrated in Fig. 21(b, c). The $\eta_{CH_4/air}$ increased to 99.8% for the perforation position of 20 mm and 97.1% for the perforation position of 30 mm. Placing the perforation position in the midstream and downstream sections of the catalytic partitioning plate may improve flame stability and $\eta_{CH_4/air}$. Regarding the flame stabilizing mechanism for the perforation locating at 20 mm and 30 mm, one may speculate that the catalytically induced gas reaction of the methane/air mixture initiates and sustains a reaction in the vicinity of the perforated wall. For some time, the wall temperature of the first stainless-

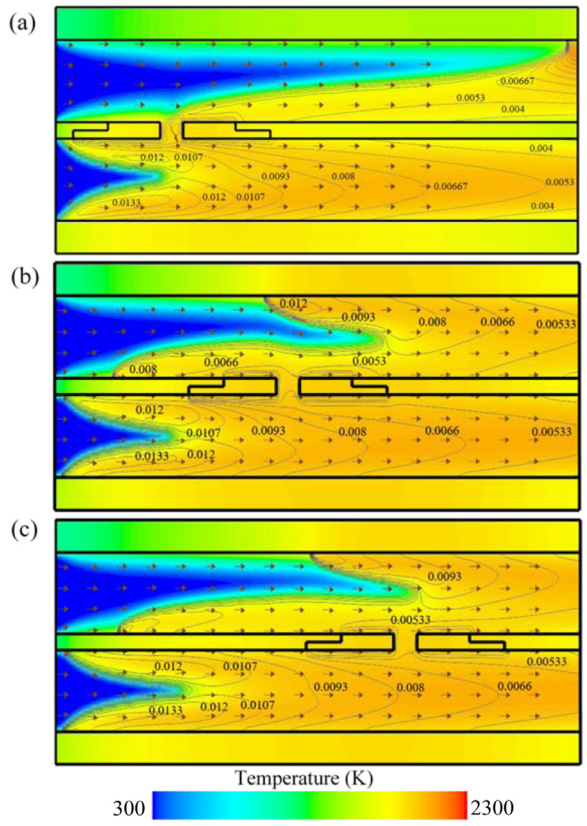

Fig. 21. Temperature distribution overlaid with OH mole fraction and velocity vectors in different perforation positions: (a) 10 mm, (b) 20 mm, (c) 30 mm.

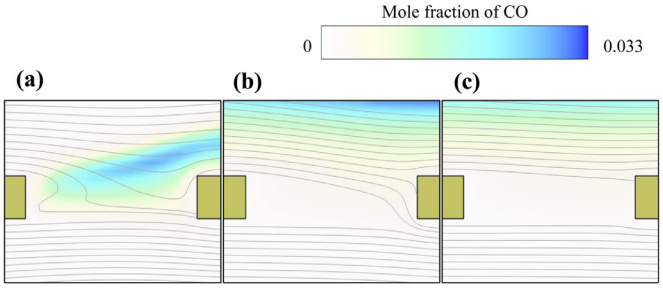

Fig. 22. CO mole fraction distribution overlaid with streamline fraction in different perforation positions: (a) 10 mm, (b) 20 mm, (c) 30 mm.

steel section increased due to the exothermicity of the homogeneous and heterogeneous reaction absorbed by the catalytic partitioning plate. The incoming methane/air mixture would be preheated by the heated wall, leading to increased flame speed. Consequently, the flame anchoring position of the methane/air mixture would flashback to the upstream stainless-steel section, as illustrated in Fig. 21(b, c).

Fig. 22 displays CO mole fraction distribution overlaid with streamline fraction in different perforation positions. When the perforation position is at x = 10 mm, the streamline presents the gas mixture from the upper channel penetrating into the lower channel, and the resulting CO is carried by the intervening flow and congregated in the perforation. In this consequence, the presence of the perforation is strongly associated with the flame stabilization of the methane/air mixture in the upper channel. Therefore, the interaction in the perforation is kinetically controlled. When the perforation position moves to 20 and 30 mm, the flow interaction in the perforation significantly diminishes, and the CO

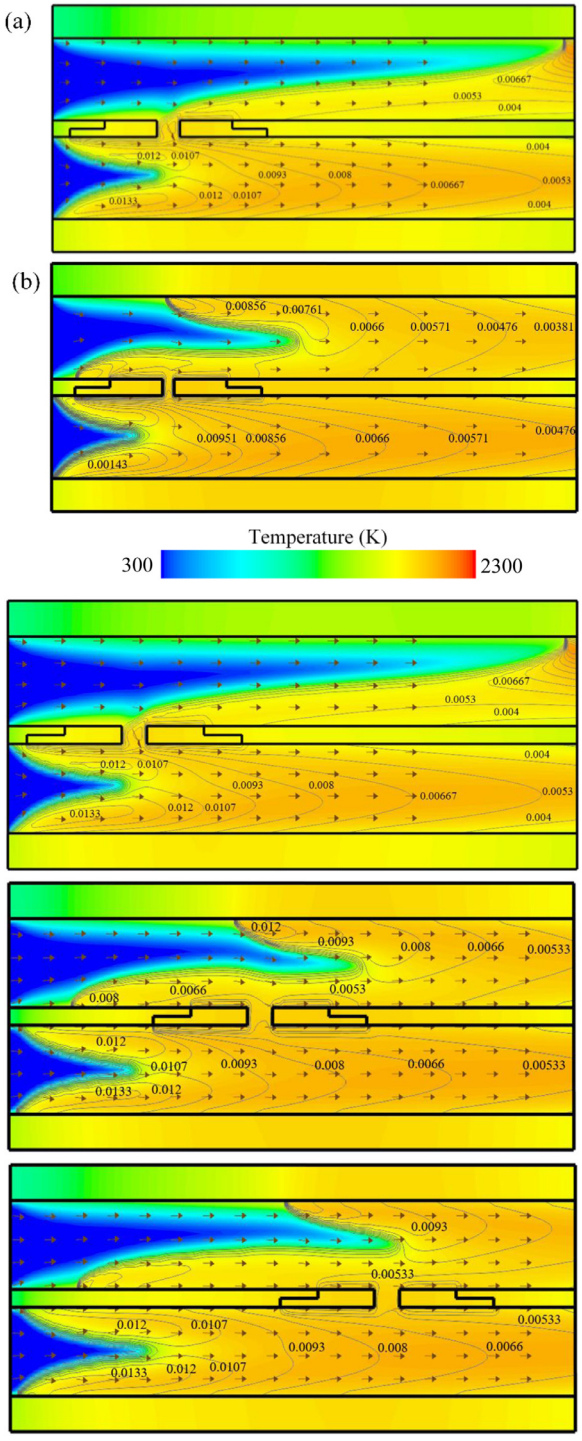

Fig. 23. Temperature distribution overlaid with OH mole fraction and velocity vector for different perforation dimensions: (a) 1 mm, (b) 2 mm.

concentration is barely diffused into the perforation, as illustrated in Fig. 22(b, c). The presence of the perforation in the middle and downstream would not arouse the disturbance in the flow fields, and the resulting CO in the perforation is attributed to mass diffusion. In this situation, the interaction in the perforation is controlled through diffusion.

Table 2

Second, the effects of the perforation dimension reduction on the flame stabilization and $\eta_{CH_4/air}$ are examined. Fig. 23 illustrates the temperature distribution overlaid with OH mole fraction

Table 2
The combustion efficiency of the methane–air mixture with different perforation positions.

Perforation position (mm)	10	20	30
$\eta_{CH_4/air}$ (%)	81.3	99.8	97.1

Table 3
The combustion efficiency of the methane/air mixture for different perforation dimensions.

Perforation size (mm)	1	2
$\eta_{CH_4/air}$ (%)	96.1	81.3

and velocity vector for different perforation dimensions (d = 1, 2 mm) when the inlet velocity of the methane/air mixture and hydrogen/air mixture are 6 and 12 m/s, respectively. The equivalence ratios for these two fuel/air mixtures are 0.8, and the heat transfer coefficient is 20 W/(m^2 K). The perforation position is at x = 10 mm, and the material of the combustor wall is stainless steel. The results in Fig. 23 reveal that the anchoring position of the catalytically induced methane/air mixture combustion moves toward the first stainless-steel section when the dimension of the perforation shrinks to 1 mm. It appears that the decrease of the perforation dimension could alleviate the imbalance of the temperature and velocity gradients around the percolated gap. Table 3 lists the $\eta_{CH_4/air}$ results for different perforation dimensions. The results illustrate a slight change in $\eta_{CH_4/air}$ as the perforation dimensions become smaller. When the dimension of the perforated gap reduces from 2 mm to 1 mm, $\eta_{CH_4/air}$ increases from 81.3% to 96.1%, resulting into 18.2% improvement in $\eta_{CH_4/air}$.

6. Conclusions

The concept of the proposed combined steel-platinum catalytic partition reactor with a percolated gap was numerically examined in this study. In order to reduce the material cost, stainless steel was chosen to replace platinum in the microreactor fabrication partially. The strategy of fuel deployment and the presence of a perforated gap on the micro combustor can effectively stabilize the flame inside the combustion chamber, resulting in a reasonable fuel conversion rate. The results demonstrate that the two different flame stabilization mechanisms appear in this research. Eventually, two approaches can curtail the effect of the presence of the perforation on the flow structure and combustion behavior, and they can further improve the $\eta_{CH_4/air}$. The most relevant results are listed as follow:

1. The simulation results demonstrated that the methane/air mixture could be effectively stabilized in the FCG compared to FCC. The methane/air flame can be anchored in the FCG in all velocity and equivalence ratio conditions due to the perforation presence. The first flame stabilization mechanism shows that the heat release region appears on the top of the perforated gap. The gas mixture from the upper channel has been penetrated the perforated gap to the lower channel. The second platinum plate in the lower channel converts CO to CO_2.
2. In the high inlet velocity of the hydrogen/air mixture and low equivalence ratio of hydrogen/air mixture condition, the hydrogen/air flame sheet extends to the bottom surface of the perforation. The high heat release of the flame sheet pushes the gas mixture in the lower channel penetrates the perforated gap. The flame sheet extends to the bottom surface of the perforated gap, resulting in pushing the gas mixture inward the perforated gap and then penetrating the upper channel and generating a recirculation zone sustained in the leading edge of the second platinum plate. The second flame stabilization mechanism shows that the formation of the recirculation zone diminished the probability of a heterogeneous reaction of derived hydrocarbon species over the second platinum plate.
3. Two approaches were proposed to contain the effect of the presence of the perforation on the flow structure and combustion behavior. First approach is to move the location of the perforation towards the downstream region and the second approach is to reduce the diameter of the perforated gap to retard the sensitivity of velocity fluctuations to the flame stabilization of the methane/air mixture. Ultimately, the resulting $\eta_{CH_4/air}$ has significantly improved in these two implementations.

Declaration of Competing Interest

All authors declared that: (i) no support, financial or otherwise, has been received from any organization that may have an interest in the submitted work; and (ii) there are no other relationships or activities that could appear to have influenced the submitted work.

CRediT authorship contribution statement

Yueh-Heng Li: Conceptualization, Funding acquisition, Methodology, Supervision, Writing - review & editing. **Kuan-Hsun Peng:** Data curation, Formal analysis, Software, Writing - original draft. **Hsiao-Hsuan Kao:** Data curation, Formal analysis, Software.

Acknowledgments

Financial support for this work was provided by the Ministry of Science and Technology (Republic of China, Taiwan) under grant numbers MOST 108-2628-E-006-008-MY3 and MOST 109-2221-E-006-037-MY3. In addition, computer time and numerical packages provided by Prof. Heiu-Jou Shaw (Department of Systems and Naval Mechatronic Engineering, National Cheng Kung University) and Prof. Wen-Lih Chen (Department of Aeronautics and Astronautics, National Cheng Kung University) are gratefully acknowledged.

References

[1] D. Dunn-Rankin, E.M. Leal, D.C. Walther, Personal power systems, Prog. Energy Combust. Sci. 31 (5–6) (2005) 422–465.
[2] A.C. Fernandez-Pello, Micropower generation using combustion: issues and approaches, Proc. Combust. Inst. 29 (1) (2002) 883–899.
[3] V.Y.R.A. Yetter, M.H. Wu, Y. Wang, D. Milius, I.A. Aksay, Combustion issues and approaches for chemical microthrusters, Adv. Energetic Mater. Chem. Propulsion (2007).
[4] C.-P. Chen, Y.-C. Chao, C.-Y. Wu, J.-C. Lee, G.-B. Chen, Development of a catalytic hydrogen micro-propulsion system, Combust. Sci. Technol. 178 (10–11) (2006) 2039–2060.
[5] H.T. Aichlmayr, D.B. Kittelson, M.R. Zachariah, Micro-HCCI combustion: experimental characterization and development of a detailed chemical kinetic model with coupled piston motion, Combust. Flame 135 (3) (2003) 227–248.
[6] Y.-H. Li, H.-W. Hsu, Y.-S. Lien, Y.-C. Chao, Design of a novel hydrogen–syngas catalytic mesh combustor, Int. J. Hydrogen Energy 34 (19) (2009) 8322–8328.
[7] Y.H. Li, G.B. Chen, H.W. Hsu, Y.C. Chao, Enhancement of methane combustion in microchannels: effects of catalyst segmentation and cavities, Chem. Eng. J. 160 (2) (2010) 715–722.
[8] V.L. Zimont, Theoretical study of self-ignition and quenching limits in a catalytic micro-structured burner and their sensitivity analysis, Chem. Eng. Sci. 134 (2015) 800–812.
[9] Y. Kizaki, H. Nakamura, T. Tezuka, S. Hasegawa, K. Maruta, Effect of radical quenching on CH4/air flames in a micro flow reactor with a controlled temperature profile, Proc. Combust. Inst. 35 (3) (2015) 3389–3396.
[10] W.-H. Chen, Y.-C. Cheng, C.-I. Hung, Transient reaction and exergy analysis of catalytic partial oxidation of methane in a Swiss-roll reactor for hydrogen production, Int. J. Hydrogen Energy 37 (8) (2012) 6608–6619.
[11] W.-H. Chen, Y.-Z. Guo, C.-C. Chen, Methanol partial oxidation accompanied by heat recirculation in a Swiss-roll reactor, Appl. Energy 232 (2018) 79–88.
[12] M. Wang, P. Li, F. Wang, Dependence of the blowout limit on flow structure, heat transfer, and pressure loss in a bluff-body micro-combustor, Int. J. Hydrogen Energy (2020).

[13] B.J. Lee, H.G. Im, Dynamics of bluff-body-stabilized lean premixed syngas flames in a meso-scale channel, Proc. Combust. Inst. 36 (1) (2017) 1569–1576.
[14] Y. Yan, Y. Liu, L. Li, Y. Cui, L. Zhang, Z. Yang, Z. Zhang, Numerical comparison of H2/air catalytic combustion characteristic of micro–combustors with a conventional, slotted or controllable slotted bluff body, Energy 189 (2019) 116242.
[15] J. Wan, H. Zhao, Flammability limit of methane-air nonpremixed mixture in a micro preheated combustor with a flame holder, Chem. Eng. Sci. 227 (2020) 115914.
[16] J. Wan, Y. Wu, H. Zhao, Excess enthalpy combustion of methane-air in a novel micro non-premixed combustor with a flame holder and preheating channels, Fuel 271 (2020) 117518.
[17] S.K. Chou, W.M. Yang, J. Li, Z.W. Li, Porous media combustion for micro thermophotovoltaic system applications, Appl. Energy 87 (9) (2010) 2862–2867.
[18] J. Li, S.K. Chou, Z.W. Li, W.M. Yang, Experimental investigation of porous media combustion in a planar micro-combustor, Fuel 89 (3) (2010) 708–715.
[19] C.-Y. Wu, S.Y. Yang, T.-C. Hsu, K.-H. Chen, Self-ignition and reaction promotion of H2 with CO2/O2 in Pt-Coated γ-Al2O3 bead reactor, Energy, 94 (2016) 524-532.
[20] T.K. Pham, D. Dunn-Rankin, W.A. Sirignano, Flame structure in small-scale liquid film combustors, Proc. Combust. Inst. 31 (2) (2007) 3269–3275.
[21] D. Shimokuri, S. Ishizuka, Flame stabilization with a tubular flame, Proc. Combust. Inst. 30 (1) (2005) 399–406.
[22] Y. Yan, H. Wang, W. Pan, L. Zhang, L. Li, Z. Yang, C. Lin, Numerical study of effect of wall parameters on catalytic combustion characteristics of CH4/air in a heat recirculation micro-combustor, Energy Convers. Manag. 118 (2016) 474–484.
[23] S.A. Smyth, K.T. Christensen, D.C. Kyritsis, Intermediate Reynolds number flat plate boundary layer flows over catalytic surfaces for “micro”-combustion applications, Proc. Combust. Inst. 32 (2) (2009) 3035–3042.
[24] A.Q. Zade, M. Renksizbulut, J. Friedman, Rarefaction effects on the catalytic oxidation of hydrogen in microchannels, Chem. Eng. J. 181-182 (2012) 643–654.
[25] R. Sui, J. Mantzaras, Combustion stability and hetero-/homogeneous chemistry interactions for fuel-lean hydrogen/air mixtures in platinum-coated microchannels, Combust. Flame 173 (2016) 370–386.
[26] C.-Y. Wu, W.-C. Yu, C.-C. Cheng, Characteristics of dimethyl ether oxidation in a preheated Pt-γ-Al2O3 catalytic reactor, Combust. Sci. Technol. (2020) 1–20.
[27] Y.-H. Li, G.-B. Chen, F.-H. Wu, T.-S. Cheng, Y.-C. Chao, Combustion characteristics in a small-scale reactor with catalyst segmentation and cavities, Proc. Combust. Inst. 34 (2) (2013) 2253–2259.
[28] Y.-H. Li, G.-B. Chen, T.-S. Cheng, Y.-L. Yeh, Y.-C. Chao, Combustion characteristics of a small-scale combustor with a percolated platinum emitter tube for thermophotovoltaics, Energy 61 (2013) 150–157.
[29] N.I. Kim, S. Kato, T. Kataoka, T. Yokomori, S. Maruyama, T. Fujimori, K. Maruta, Flame stabilization and emission of small Swiss-roll combustors as heaters, Combust. Flame 141 (3) (2005) 229–240.
[30] S. Wang, Z. Yuan, A. Fan, Experimental investigation on non-premixed CH4/air combustion in a novel miniature Swiss-roll combustor, Chem. Eng. Process. - Process Intensification 139 (2019) 44–50.
[31] W. Wang, Z. Zuo, J. Liu, Numerical study of the premixed propane/air flame characteristics in a partially filled micro porous combustor, Energy 167 (2019) 902–911.
[32] W.M. Yang, S.K. Chou, K.J. Chua, J. Li, X. Zhao, Research on modular micro combustor-radiator with and without porous media, Chem. Eng. J. 168 (2) (2011) 799–802.
[33] Z. He, Y. Yan, S. Feng, X. Li, Z. Yang, J. Ran, Y. Gan, Investigation on premixed methane/air combustion characteristics in heat recirculation micro combustor with separating cylinder, Chem. Eng. Process. - Process Intensification 153 (2020) 107987.
[34] J. Wan, A. Fan, H. Yao, W. Liu, Flame-anchoring mechanisms of a micro cavity–combustor for premixed H2/air flame, Chem. Eng. J. 275 (2015) 17–26.
[35] J. Pan, Q. Lu, S. Bani, A. Tang, W. Yang, X. Shao, Hetero-/homogeneous combustion characteristics of premixed hydrogen-air mixture in a planar micro-reactor with catalyst segmentation, Chem. Eng. Sci. 167 (2017) 327–333.
[36] K. Maruta, K. Takeda, J. Ahn, K. Borer, L. Sitzki, P.D. Ronney, O. Deutschmann, Extinction limits of catalytic combustion in microchannels, Proc. Combust. Inst. 29 (1) (2002) 957–963.
[37] Y.-T. Wu, Y.-H. Li, Combustion characteristics of a micro segment platinum tubular reactor with a gap, Chem. Eng. J. 304 (2016) 485–492.
[38] J. Chen, X. Gao, D. Xu, Kinetic effects of hydrogen addition on the catalytic self-ignition of methane over platinum in micro-channels, Chem. Eng. J. 284 (2016) 1028–1034.
[39] H. Daneshvar, R. Prinja, N.P. Kherani, Thermophotovoltaics: Fundamentals, challenges and prospects, Appl. Energy 159 (2015) 560–575.
[40] Y.-H. Li, J.-R. Hong, Performance assessment of catalytic combustion–driven thermophotovoltaic platinum tubular reactor, Appl. Energy 211 (2018) 843–853.
[41] Y.H. Li, Y.S. Lien, Y.C. Chao, D. Dunn-Rankin, Performance of a mesoscale liquid fuel-film combustion-driven TPV power system, Prog. Photovoltaics 17 (5) (2009) 327–336.
[42] Y.-H. Li, T.-S. Cheng, Y.-S. Lien, Y.-C. Chao, Development of a tubular flame combustor for thermophotovoltaic power systems, Proc. Combust. Inst. 33 (2) (2011) 3439–3445.
[43] Y.-H. Li, C.-Y. Wu, Y.-S. Lien, Y.-C. Chao, Development of a high-flame-luminosity thermophotovoltaic power system, Chem. Eng. J. 162 (1) (2010) 307–313.
[44] Y.-H. Li, Y.-C. Chao, N.S. Amadé, D. Dunn-Rankin, Progress in miniature liquid film combustors: double chamber and central porous fuel inlet designs, Exp. Therm. Fluid Sci. 32 (5) (2008) 1118–1131.
[45] S. Chadha, R. Jefferson-Loveday, T. Hussain, Modelling Knudsen number effects in suspension high velocity oxy fuel thermal spray, Int. J. Heat Mass Transf. 152 (2020) 119454.
[46] J. Wan, A. Fan, Effect of solid material on the blow-off limit of CH4/air flames in a micro combustor with a plate flame holder and preheating channels, Energy Convers. Manag. 101 (2015) 552–560.
[47] D. Shi, F. Zou, Z. Zhu, J. Sun, Modeling the effect of surface oxidation on the normal spectral emissivity of steel 316L at 1.5μm over the temperatures ranging from 800 to 1100K in air, Infrared Phys. Technol. 71 (2015) 370–377.
[48] W. Sabuga, R. Todtenhaupt, Effect of roughness on the emissivity of the precious metals silver, gold, palladium, platinum, rhodium, and iridium, High Temperatures High Pressures(UK) 33 (3) (2001) 261–269.
[49] J. Warnatz, M.D. Allendorf, R.J. Kee, M.E. Coltrin, A model of elementary chemistry and fluid mechanics in the combustion of hydrogen on platinum surfaces, Combust. Flame 96 (4) (1994) 393–406.
[50] R.S. Amano, M.M. Abou-Ellail, S. Elhaw, M.S. Ibrahim, Numerical simulation of hydrogen–air reacting flows in rectangular channels with catalytic surface reactions, Heat Mass Transf. 49 (9) (2013) 1243–1260.
[51] M. Reinke, J. Mantzaras, R. Bombach, S. Schenker, A. Inauen, Gas phase chemistry in catalytic combustion of methane/air mixtures over platinum at pressures of 1 to 16 bar, Combust. Flame 141 (4) (2005) 448–468.
[52] O. Deutschmann, L.I. Maier, U. Riedel, A.H. Stroemman, R.W. Dibble, Hydrogen assisted catalytic combustion of methane on platinum, Catal. Today 59 (1–2) (2000) 141–150.
[53] R. Sui, E.-tt. Es-sebbar, J. Mantzaras, N.I. Prasianakis, Experimental and numerical investigation of fuel-lean H2/CO/air and H2/CH4/air catalytic microreactors, Combust. Sci. Technol. 190 (2) (2018) 336–362.
[54] R. Sui, J. Mantzaras, Combustion stability and hetero-/homogeneous chemistry interactions for fuel-lean hydrogen/air mixtures in platinum-coated microchannels, Combust. Flame 173 (Supplement C) (2016) 370–386.
[55] S. Karagiannidis, J. Mantzaras, Numerical investigation on the start-up of methane-fueled catalytic microreactors, Combust. Flame 157 (7) (2010) 1400–1413.